



## Research Papers

# An acid microenvironment-driven theranostics platform for lung cancer $^{19}\text{F}$ MR/PA/FL multimodal imaging-guided photothermal therapy

Maosong Qiu, Lei Zhang, Yu Li, Ruifang Wang, Long Xiao, Shizhen Chen\*, Xin Zhou\*

Key Laboratory of Magnetic Resonance in Biological Systems, State Key Laboratory of Magnetic Resonance and Atomic and Molecular Physics, National Center for Magnetic Resonance in Wuhan, Wuhan Institute of Physics and Mathematics, Innovation Academy for Precision Measurement Science and Technology, Chinese Academy of Sciences, Wuhan National Laboratory for Optoelectronics, Huazhong University of Science and Technology (HUST), Wuhan 430071, China



## ARTICLE INFO

## Keywords:

$^{19}\text{F}$  MRI  
Photoacoustic imaging  
Fluorescence imaging  
pH-responsive  
Photothermal therapy

## ABSTRACT

Enhancing the tumor-to-background ratio in multimodal imaging to achieve precise tumor localization remains a pivotal objective for effective and specific photothermal therapy (PTT). However, developing tumor microenvironment-responsive multimodal probes for imaging-guided tumor therapy remains a formidable challenge. Herein, we engineered IR820-loaded fluorinated zeolitic imidazolate frameworks (ZIF-8) coated gold nanorod (GFZI) for FL/PA/ $^{19}\text{F}$  MR trimodal-guided PTT in lung cancer. Upon reaching the tumor site, these nanoparticles trigger an enhancement in fluorescence imaging and  $^{19}\text{F}$  magnetic resonance imaging, facilitated by the controlled release of IR820 and 4-(trifluoromethyl)-1H-imidazole. Furthermore, GFZI undergoes degradation in the acidic tumor microenvironment, exposing the gold nanorods, thereby amplifying the photoacoustic signal and photothermal therapy. The amalgamation of acidic-activated FL/PA/ $^{19}\text{F}$  MR trimodal imaging techniques ensures precise localization of lung cancer, realizing the outstanding PTT effect of lung cancer. This versatile platform holds great promise for achieving precision in cancer theranostics, offering new avenues in cancer diagnosis and treatment.

## 1. Introduction

Lung cancer is the most common cancer and the leading cause of death worldwide [1]. Due to the limited availability of accurate detection techniques, most lung cancers are diagnosed at advanced stages (stage III/IV) [2]. Widely used low-dose computed tomography (CT) screening has reduced lung cancer mortality [3], but it suffers from ionizing radiation and a high false-positive rate of 96.4% [4]. Compared with single imaging technology, multimodal imaging utilizes the merits of complementary imaging modalities to achieve the precise location of the tumor. Heretofore, positron emission tomography (PET)/magnetic resonance imaging (MRI) and PET/CT have been widely used for precise diagnosis of tumors in clinical [5]. Except for PET and CT, fluorescence imaging (FLI) exhibits ultra-high sensitivity, and photoacoustic imaging (PAI) is suitable for the evaluation of tumor penetration [6,7], which could be used to compensate for the low sensitivity of MRI [8]. In addition,  $^{19}\text{F}$  MRI affords incomparable spatial resolution and almost no endogenous interference [9–11]. By exploiting the complementarity of  $^{19}\text{F}$  MRI and FLI, Chen et al. designed a novel probe for the accurate detection of orthotopic lung cancer [12]. Besides, Zhang et al. proposed

a versatile theranostic for precise FL/PA/ $^{19}\text{F}$  MR trimodal-guided photodynamic therapy [13]. However, all the theranostics with  $^{19}\text{F}$  MR/FL/PA trimodal-guided photothermal or photodynamic therapy of tumors possess an "always-on" multimodal imaging signal, leading to low tumor-to-background ratios (TBR) [14,15]. Addressing the aforementioned issue, there is a pressing demand for the advancement of non-ionizing radiation and dependable theranostics to enable precise therapy for lung cancer, guided by activatable multimodal imaging.

Based on the mild acid tumor microenvironment (TME), the acid-activated theranostics were designed for multimodal imaging-guided precise therapy [16–18]. Zeolitic imidazolate framework-8 (ZIF-8) is one of the most commonly used metal-organic frameworks [19]. With the ability of drug-loading and acid-responsive degradability, ZIF-8 has been widely used in biomedical applications [20]. In virtue of the drug encapsulation and delivery, Chen et al. synthesized ZIF-8 loading with ICG for the FLI-guided photothermal therapy (PTT) of hepatic carcinoma [21]. Besides, Liang et al. synthesized a nanohybrid based on  $\text{Fe}_3\text{O}_4$  coated with ZIF-8 for *in vivo*  $T_1/T_2$  dual-modal MRI [22]. To endow the performance of  $^{19}\text{F}$  MRI, the researchers prepared ZIF-8 by partly replacing 2-methylimidazole (2-MIM) with

\* Corresponding authors.

E-mail addresses: [chenshizhen@wipm.ac.cn](mailto:chenshizhen@wipm.ac.cn) (S. Chen), [xinzhou@wipm.ac.cn](mailto:xinzhou@wipm.ac.cn) (X. Zhou).

<https://doi.org/10.1016/j.matresbull.2024.112731>

Received 5 December 2023; Received in revised form 15 January 2024; Accepted 9 February 2024

Available online 10 February 2024

0025-5408/© 2024 Elsevier Ltd. All rights reserved.

4-(trifluoromethyl)-1H-imidazole (TFMIM), achieving the acid-activated  $^{19}\text{F}$  MRI or  $^{19}\text{F}$  MRI-guided immunotherapy of tumors [23,24]. By designing TME-responsive nanoprobe for multimodal imaging-guided precise therapy is highly desirable. However, great challenges remain in developing smart and activated multimodal nanoprobe for precision theranostics on demand, leading to the scarcity of versatile nanoplatforms based on ZIF-8 for acid-responsive multimodal imaging-guided therapy of tumors. Therefore, the rational design of the ZIF-8 nanohybrid has great significance for the activated imaging-guided precise therapy of lung cancer.

Herein, the acid-driven core-shell nanoplatform based on fluorinated ZIF-8 coated on gold nanorods (GNRs) was fabricated for the  $^{19}\text{F}$  MR/FL/PA trimodal imaging-guided lung cancer PTT (Fig. 1). In detail, GNRs endow nanoplatform with a preeminent performance of PAI and PTT [25]. Coating with fluorinated ZIF-8 (F-ZIF-8) by partially replacing 2-MIM with TFMIM, which endows GNR@F-ZIF-8 (GFZ) with  $^{19}\text{F}$  MRI performance. With the loading of IR820 (GNR@F-ZIF-8@IR820, denoted as GFZI), the nanoplatform was further functionalized with FLI capability and a better photothermal effect. After being modified with Pluronic F127, the as-fabricated nanoplatform displayed good dispersibility in a buffer solution. When delivered to the tumor region via the enhanced permeability and retention (EPR) effect, F-ZIF-8 could collapse in the acidic TME, leading to the release of TFMIM and IR820 and the exposure of GNRs, thus realizing the enhancement of  $^{19}\text{F}$  MR/FL/PA trimodal imaging contrast, which is conducive to guide the subsequent PTT precisely. Moreover, the better PTT efficiency of lung cancer was obtained due to the synergistic photothermal effect of gold nanorods and IR820. Multimodal imaging technology provides great opportunities for the precise location of tumors [26]. Notably, there were only three reported probes equipped with the capacity of  $^{19}\text{F}$  MR/PA/FL trimodal imaging [13–15], suggesting the great challenge in the preparation of  $^{19}\text{F}$  MR/PA/FL trimodal probes. In this work, a novel strategy for the fabrication of a responsive  $^{19}\text{F}$  MR/PA/FL trimodal nanoprobe was proposed, achieving the TME-responsive enhancement of  $^{19}\text{F}$  MR/FL/PA trimodal imaging and dually augmented PTT for lung cancer theranostic.

## 2. Experimental section

### 2.1. Preparation of GNR@F-ZIF-8 core-shell nanoparticles

The GNRs were prepared using a previously reported method [27]. After the successful synthesis of GNRs, the CTAB coated on the GNRs was replaced by the PVP (K30). Then, 4 mL of GNRs and 8 mL of a methanol solution containing the 2-MIM (14.25 mg), and TFMIM (3.56 mg) were mixed with stirring for 5 min. 8 mL of a methanol solution containing  $\text{Zn}(\text{NO}_3)_2 \cdot 6\text{H}_2\text{O}$  (30.38 mg) was introduced to the above solution and stood for 1 h. After that, the product was centrifugated at 10,000 rpm for 10 min, washed with methanol three times, and finally obtained GNR@F-ZIF-8 nanoparticles (GFZ). Then, 1 mg IR820 or FITC was added to the GFZ solution. After sonicating for 3 min and stirring for 12 h without light, GFZ@IR820 (GFZI) or GFZ@FITC (GFZF) was obtained by centrifugation at 10,000 rpm for 10 min. Finally, the biocompatibility of GFZI or GFZF was further improved by the modification with Pluronic F127.

### 2.2. *In vitro* and *in vivo* PAI

The PAI experiments were carried out on a real-time multispectral optoacoustic tomographic system (iThera Medical, Germany). The cellular PAI was performed on the A549 cells and MRC-5 cells after incubation with GFZI (100  $\mu\text{g}/\text{mL}$ ) for 6 h, respectively. After that, the PA intensity of cells was determined. *In vivo* PAI was conducted on the A549 tumor-bearing mice at various times after *i.v.* injection of GFZI (200  $\mu\text{g}/\text{mL}$ , 100  $\mu\text{L}$ ).

### 2.3. *In vitro* and *in vivo* $^{19}\text{F}$ MRI

The  $^{19}\text{F}$  MRI experiments were performed on a 9.4 T micro-imaging system (Bruker Avance 400, Ettlingen, Germany). The *in vitro*  $^{19}\text{F}$  MR images were obtained via the RARE method (TR = 500 ms, TE = 3 ms, FOV = 3 cm  $\times$  3 cm, 25 mm slice thickness, RARE factor = 4, matrix size = 32  $\times$  32, ns = 128). For the cellular  $^{19}\text{F}$  MRI, the A549 cells and MRC-5 cells were incubated with different concentrations of GFZI for 6 h. Then,

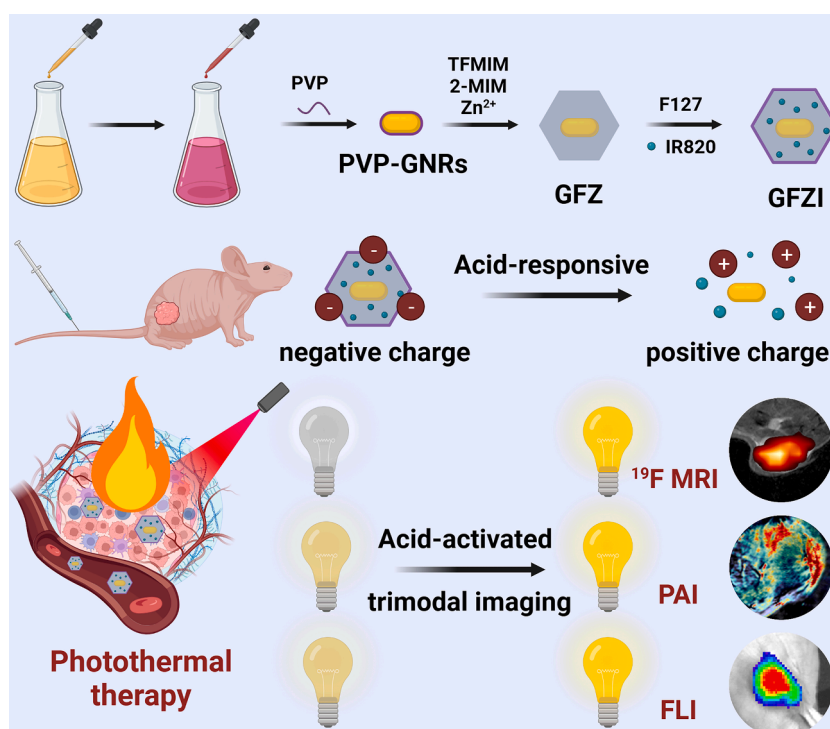


Fig. 1. Schematic of the preparation of GFZI for acid-responsive  $^{19}\text{F}$  MR/PA/FL multimodal imaging-guided photothermal therapy.

the cellular  $^{19}\text{F}$  MRI was carried out after treatment with RIPA lysate. For the *in vivo*  $^{19}\text{F}$  MRI, the subcutaneous A549 tumor-bearing mice were intratumorally injected with 50  $\mu\text{L}$  of GFZI (200  $\mu\text{g}/\text{mL}$ ). After a  $^1\text{H}$  MRI scan using a RARE sequence (TR = 2500 ms, TE = 33 ms, FOV = 4.0 cm  $\times$  4.0 cm, 1 mm slice thickness, RARE factor = 8, matrix size = 256  $\times$  256), the  $^{19}\text{F}$  MRI was performed through a RARE sequence at time points of 0.5 h, 2 h, and 4 h post-injection, respectively. (TR = 800 ms, TE = 3 ms, FOV = 4.94 cm  $\times$  4.94 cm, 18.5 mm slice thickness, matrix size = 32  $\times$  32, ns = 64).

#### 2.4. *In vivo* fluorescence imaging

The FLI was conducted on an IVIS Spectrum imaging system (Perkin Elmer) (Ex: 740 nm; Em: 820 nm). Upon the tumor growing to about 150  $\text{mm}^3$ , the FLI was performed at different time points after the A549 tumor-bearing mice were *i.v.* injection with GFZI (200  $\mu\text{g}/\text{mL}$ , 100  $\mu\text{L}$ ).

After 12 h post-injection of GFZI, the mice were sacrificed to extract the heart, liver, spleen, lungs, kidneys, and tumors. *Ex vivo* FLI was performed for semiquantitative biodistribution analysis.

#### 2.5. *In vivo* antitumor effect

When the A549 tumor volume reached approximately 100  $\text{mm}^3$ , the nude mice were divided into five groups ( $n = 4$ ) with the therapy of (I) PBS plus laser, (II) IR820 plus laser, (III) GFZI, (IV) GFZ plus laser, (V) GFZI plus laser. The dose of the tail vein injection was set as 200  $\mu\text{g}/\text{mL}$  (100  $\mu\text{L}$ ). The mice in all groups received tail vein injections of PBS, GFZ, or GFZI (200  $\mu\text{g}/\text{mL}$ , 100  $\mu\text{L}$ ) at day 0. After 12 h post-injection, the groups plus laser suffered from 808 nm laser (1.0  $\text{W}/\text{cm}^2$ ) twice for 5 min (5 min apart). The temperature change in the tumor region was recorded by a NIR thermal imager. The treated mice on different days were photographed for the observation of PTT efficacy. The tumor

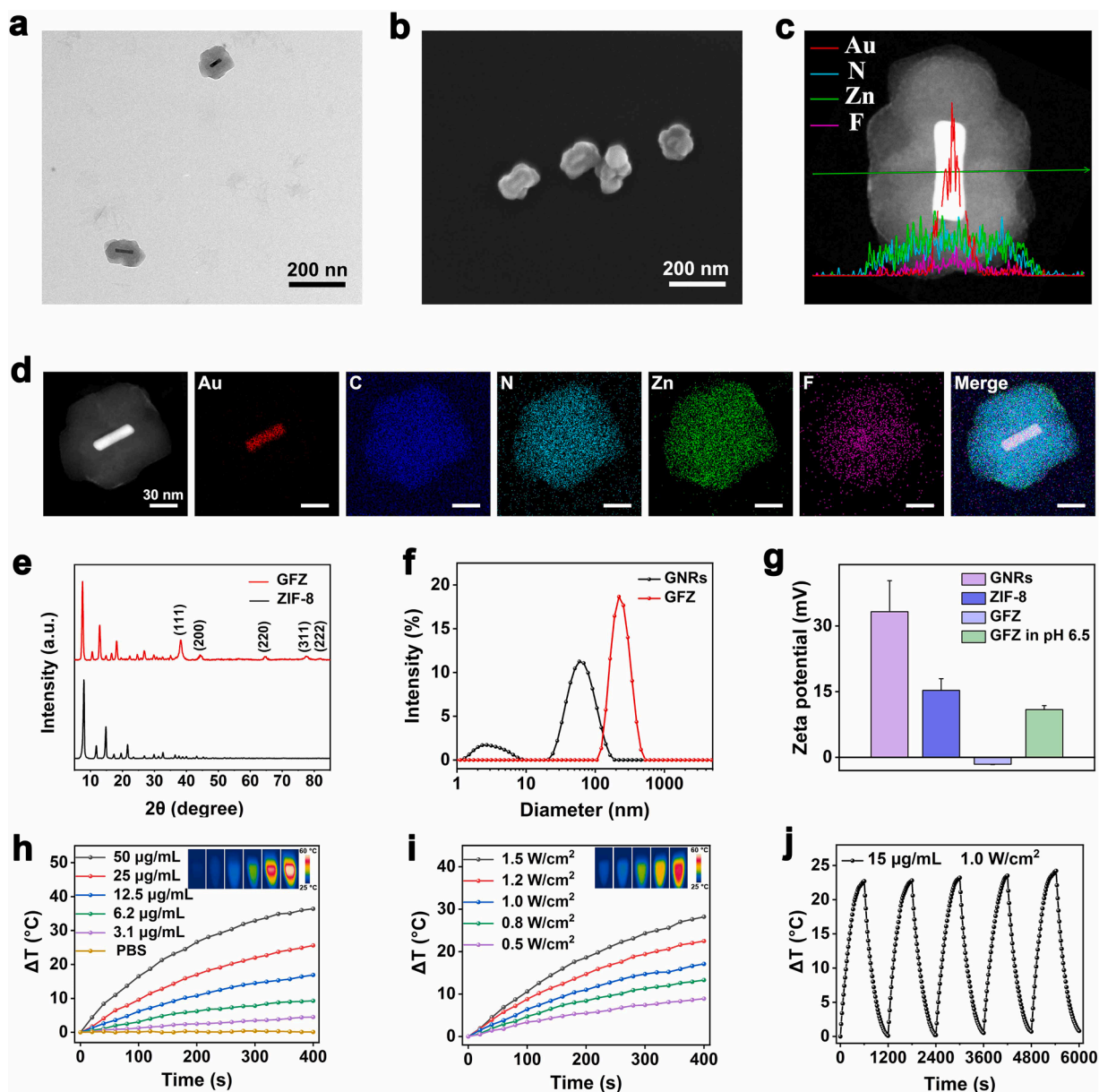


**Fig. 2.** Characterization of GFZ. (a) TEM image of GFZ. (b) SEM image and (c) corresponding cross-sectional compositional line profiles of GFZ. (d) Elemental mapping of GFZ. (e) XRD of GFZ. (f) Size distribution of GNRs and GFZ. (g) Zeta potential of GNRs, ZIF-8, and GFZ. (h) The photothermal effect of GFZ in PBS at different gold nanorod concentrations (808 nm, 1.0  $\text{W}/\text{cm}^2$ ). (i) Photothermal effect of GFZ ( $C_{\text{Au}} = 12.5 \mu\text{g}/\text{mL}$ ) under 808 nm laser with different power densities. (j) Photothermal stability of GFZ ( $C_{\text{Au}} = 15 \mu\text{g}/\text{mL}$ ) within five cycles of 808 nm laser irradiation (1.0  $\text{W}/\text{cm}^2$ ).

volume (TV) and the body weight of mice were recorded every two days. The TV was calculated via the formula:  $TV = \text{length} \times \text{width}^2/2$ . Relative tumor volume was calculated as  $V_n/V_0$ , where  $V_n$  and  $V_0$  are the tumor volume measured at Day  $n$  and Day 0, respectively.

### 3. Results and discussion

#### 3.1. Characterization of nanoparticles

Firstly, the CTAB-stabilized GNRs were synthesized via seed-mediated protocol [27]. The transmission electron microscopy (TEM) image unveiled GNRs with an impressively uniform size of about  $50 \times 17$  nm (length  $\times$  width) (Fig. S1). After replacing CTAB with PVP, we introduced 2-MIM, TFMIM, and  $Zn(NO_3)_2 \cdot 6H_2O$  into the solutions. This meticulous process resulted in the creation of monodisperse core-shell GFZ nanoparticles, maintaining a consistent size of approximately 100 nm. This successful fabrication was verified through TEM and SEM images (Fig. 2a, b). Further confirmation was provided by cross-sectional compositional line profiles (Fig. 2c) and elemental mapping (Fig. 2d) of GFZ, illustrating the existence of Au, C, N, Zn, and F elements, as corroborated by the X-ray photoelectron spectroscopy (XPS) spectrum (Fig. S2). These results establish the triumph of the core-shell GFZ synthesis. Beyond morphology, the X-ray diffraction (XRD) pattern of GFZ closely resembled that of ZIF-8. The diffraction peaks at 38.28, 44.34, 64.57, 77.44, and 81.79 were corresponding to the (111), (200), (220), (311), and (222) crystal facets of Au (JCPDS 00-004-0784) (Fig. 2e) [28]. With the application of a fluorinated-ZIF-8 coating onto the GNRs, the average hydrodynamic diameter was increased from 67 nm to 241 nm (Fig. 2f). In contrast to the positive potential exhibited by GNRs and ZIF-8, GFZ displayed a negative zeta potential. Upon incubation in a slightly acidic PBS solution (pH = 6.5), the zeta potential of GFZ shifted to positive values (Fig. 2g), facilitating cellular uptake within the TME [29]. Furthermore, the UV-Vis-NIR absorption spectra of GNRs showcased a notable bathochromic shift with the decoration of the fluorinated ZIF-8 (Fig. S3) due to the change of refractive index surrounding the GNRs, consistent with findings in the

literature [30]. The reduction of UV-Vis-NIR absorption in 800–900 nm is similar to the literature results [27,31], which may be the change in the surrounding environment of GNRs and a small portion of gold nanorods undergo aggregation. The coating of fluorinated ZIF-8 leads to the attenuation of UV-Vis-NIR absorption, which would reduce the photothermal effect of GFZI. However, upon the fluorinated ZIF-8 collapse in an acid environment, the enhancement of UV-Vis-NIR absorption and photothermal effect may be realized. Finally, we evaluated the photothermal conversion performance of GFZ, revealing a significant correlation with both laser irradiation power densities and concentrations (Fig. 2h, i). The outstanding photothermal stability of GFZ was confirmed through five cycles of laser on-off processes (Fig. 2j). The photothermal conversion efficiency of GFZ was calculated as 23.8 % by using our previous method (Fig. S4) [32], which is similar to the literature report [33]. Upon loading with IR820, the GFZI group exhibited higher temperature elevations during laser irradiation compared to both the GFZ and IR820 groups (Fig. S5), affirming the synergistic photothermal effect of gold nanorods and IR820.

#### 3.2. *In vitro* pH-activated $^{19}F$ MRI/PAI and photothermal therapy

The incorporation of TFMIM into GFZI conferred it with the ability to perform  $^{19}F$  MRI. Given ZIF-8's inherent acid-sensitive degradation characteristics, we explored the acid-responsive  $^{19}F$  MRI capabilities of GFZI. As anticipated, the  $^{19}F$  NMR signal, initially registering at  $-61.9$  ppm, remained relatively subdued at a pH level of 7.4. However, it exhibited a notable increase as the pH value decreased (Fig. 3a). To assess GFZI's acid-responsive  $^{19}F$  MRI performance, we conducted phantom studies. The  $^{19}F$  MR imaging of GFZI solutions, varying in concentration and subjected to different pH conditions, revealed the emergence of "hot spot" images under acidic conditions, accompanied by a concentration-dependent augmentation in  $^{19}F$  MRI signal intensity (Fig. 3b, 3c). This observation holds significant promise for the *in vivo* application of GFZI in  $^{19}F$  MRI. Beyond the enhancement in  $^{19}F$  MRI signal intensity, the degradation of GFZI exposed the GNRs, resulting in a substantial increase in UV-Vis-NIR absorption within the 800–900 nm

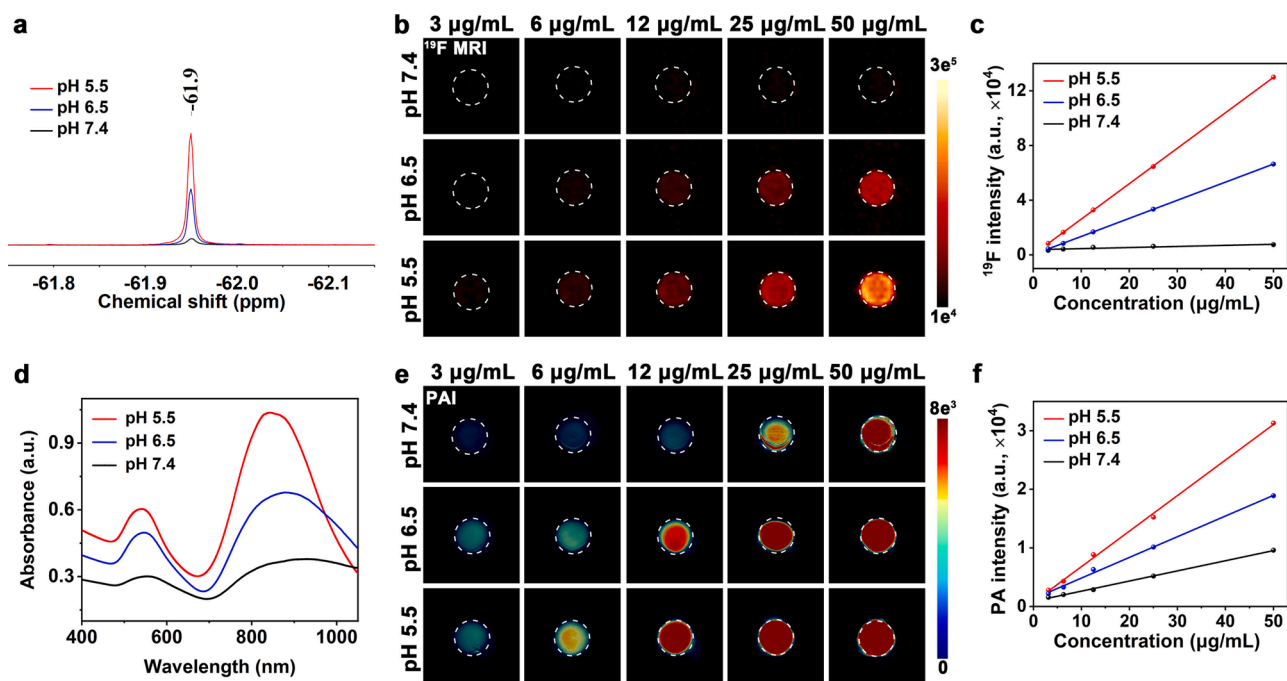


**Fig. 3.** *In vitro*  $^{19}F$  MRI and PAI of GFZI. (a)  $^{19}F$  NMR spectra of GFZI. (b)  $^{19}F$  MRI of GFZI aqueous solution with various concentrations under different pH values and (c) the corresponding relationship between signal intensity and GFZI concentrations. (d) UV-Vis-NIR spectrum of GFZI aqueous solution under different pH values. (e) PAI of GFZI aqueous solution with various concentrations under different pH values and (f) the corresponding relationship between signal intensity and GFZI concentrations.

range (Fig. 3d). The principle of PAI hinges on the photoacoustic effect of light-absorbing agents. Thanks to the acid-responsive amplification of UV-Vis-NIR absorption, we obtained high-contrast images with a concentration-dependent enhancement in PAI signal intensity (Fig. 3e, 3f).

Encouraged by the exceptional performance of GFZI in phantom-based  $^{19}\text{F}$  MR/PA dual-modal imaging, we proceeded to assess its cellular imaging capabilities. Initially, we scrutinized the intracellular uptake of GFZI in A549 and MRC-5 cells using confocal laser scanning microscopy (CLSM). To study the time-dependent cellular endocytosis of GFZ nanoparticles loaded with FITC (GFZF), we examined A549 cells. The fluorescence intensity increased with extended incubation times and reached a saturation point within 6 h (Figs. S6, S7). We also constructed 3D tumor spheroids using LLC cells (due to the challenges in preparing 3D A549 tumor spheroids) to evaluate the penetration capacity of GFZF. Intriguingly, after incubation at pH 6.5 for 2 h, GFZF dispersed throughout the LLC cells-based multicellular spheroids (MCSs). Moreover, the infiltration efficacy increased further at pH 5.5 after 2 h post-incubation, as evidenced by strong green fluorescence distributed widely across the entire MCSs. This confirmed the acid-enhanced tumor infiltration capabilities of GFZF. In contrast, at pH 7.4 after 2 h post-incubation, GFZF was retained at the outer border of MCSs (Fig. 4a). These findings collectively demonstrate that GFZF possesses robust tumor penetration capabilities, which are pivotal for overcoming biological barriers and enhancing drug delivery efficiency. We then studied the differences in GFZF uptake between A549 and MRC-5 cells. CLSM and flow cytometry analysis results revealed that A549 cells internalized GFZF to a much greater extent than MRC-5 cells after 6 h of incubation (Figs. S8, S9), indicating the significant potential of GFZI in tumor photothermal therapy.

Subsequently, cellular-level  $^{19}\text{F}$  MR/PA dual-modal imaging was conducted on both A549 and MRC-5 cells. Due to the high uptake efficiency in A549 cells,  $^{19}\text{F}$  MRI exhibited a much more pronounced contrast effect compared to MRC-5 cells after incubation with GFZI. An evident positive correlation between  $^{19}\text{F}$  MRI signal intensity and GFZI concentrations was observed in A549 cells, while a weaker positive correlation was noted in MRC-5 cells (Fig. 4b). The reasons for the activation of cellular  $^{19}\text{F}$  MRI may be attributed from the collapse of GFZI in lysosomes and the cells were lysed by RIPA lysate further increased the transverse relaxation time ( $T_2$ ) of TFMIM. Furthermore, the cellular PAI findings aligned with the  $^{19}\text{F}$  MRI results (Fig. 4c), ensuring precise MRI/PAI dual-modal detection of lung cancer. It is worth noting that the excellent PAI signal could be obtained without the collapse of GFZI (Fig. 3e), thus the outstanding A549 cellular PAI signal was reasonable without lysing by the RIPA lysate.

Beyond cancer cell imaging, we proceeded to conduct photothermal therapy at the cellular level. Before therapy, we evaluated the cytotoxicity of GFZI. Even at concentrations up to 200  $\mu\text{g}/\text{mL}$ , the cell survival rate of both A549 and MRC-5 cells showed no significant decrease (Fig. S10). However, upon 10 min of continuous laser irradiation (808 nm, 1.0  $\text{W}/\text{cm}^2$ ), significant concentration-dependent reductions in A549 cell viability were observed compared to MRC-5 cells (Fig. S11). Calcein-AM/PI labeled A549 cells were further used to visualize the anticancer activity of GFZI by CLSM imaging. In the groups treated with PBS, PBS plus laser, and GFZI, the ignorable dead cells displaying red fluorescence were observed. In contrast, the obvious dead cells were observed in the laser-irradiated area after incubation with GFZI (Fig. 4d). Flow cytometry analysis of Annexin V-FITC/PI staining of cells further confirmed that GFZI-induced PTT led to apoptosis in A549 cells (Fig. 4e).

### 3.3. *In vivo* pH-responsive FL/PA/ $^{19}\text{F}$ MR tri-modal imaging

To validate the *in vivo* imaging capabilities of GFZI, we conducted acidic-triggered activation of fluorescence, photoacoustic, and  $^{19}\text{F}$  MR contrast in subcutaneous A549 tumor-bearing mice. Hemolysis test

results, indicating a rate of less than 5%, confirmed the excellent biocompatibility and injection safety of GFZI (Fig. S12). Following the intravenous injection of GFZI, FLI revealed an initial accumulation of GFZI in the liver region, followed by gradual accumulation in the tumor region (Fig. 5a). Quantitative FLI analysis demonstrated that GFZI achieved its highest tumor accumulation at the 12 h post-injection mark (Fig. 5c). This suggests that GFZI possessed favorable passive tumor targeting capabilities via the EPR effect, a crucial factor in PTT.

Subsequently, FLI and quantitative analysis of both the tumor and main organs harvested at the 12 h post-injection point confirmed that tumor site accumulation was second only to the liver, further affirming the efficient tumor accumulation of GFZI (Fig. 5b, d). Additionally, the PA signal peaked at 12 h post-injection of GFZI, with the tumor's peak PA intensity being approximately 2.8-fold higher than that observed at 2 h post-injection. This result further validated the optimal tumor accumulation of GFZI at the 12 h time point (Fig. 5e, f). To further corroborate the acidic-responsive enhancement of *in vivo* imaging, we performed the  $^{19}\text{F}$  MRI of the tumor by intratumoral injection of GFZI. The  $^{19}\text{F}$  MRI signal at the tumor site, assessed 0.5 h post-injection, exhibited significantly higher contrast than that in normal tissue, and the signal completely vanished at 4 h after injection (Fig. 5g). These findings collectively demonstrate that GFZI can achieve acidic-responsive enhancement of imaging signals and effectively accumulate in tumor tissue, thus ensuring the efficacy of *in vivo* PTT.

### 3.4. *In vivo* imaging-guided PTT

Leveraging the robust tumor accumulation and the multimodal imaging capabilities encompassing FL/PA/ $^{19}\text{F}$  MR, we embarked on imaging-guided PTT for xenograft lung cancer using GFZI. As the tumor size reached approximately 100  $\text{mm}^3$ , five groups of A549 tumor-bearing BALB/c nude mice ( $n = 4$ ) underwent treatment: (group I) PBS + NIR laser, (group II) IR820 + NIR laser, (group III) GFZI only, (group IV) GFZ + NIR laser, and (group V) GFZI + NIR laser. To monitor treatment progress, we photographed the mice on different days and recorded tumor volumes and body weight every two days for 14 days.

In line with the *in vivo* FL and PA images (Fig. 5a, e), we opted to implement PTT at the 12 h post-injection mark. When exposed to 808 nm laser for 5 min, the tumor region's temperature in group V rose to 51.2  $^{\circ}\text{C}$ , indicating a more potent photothermal effect compared to the 47.7  $^{\circ}\text{C}$  observed in group IV, attributed to the synergistic enhancement of photothermal efficacy between GNRs and IR820. In contrast, the temperature changes in groups I-III were insufficient to cause tumor cell damage (Fig. S13). Significant inhibition of tumor growth was observed in groups IV and V compared to groups I-III. Without an 808 nm laser, GFZI exhibited negligible antitumor effect, suggesting the low inherent toxicity of nanoparticle components (Fig. 6a).

On day 14, the excised tumors were photographed and weighed. Remarkably, half of the tumors in group V were completely ablated (Fig. 6b). Both the size and the mass of the tumor demonstrated excellent PTT effect in group V, with  $p < 0.001$  and 0.05 compared to group II and group IV, respectively (Fig. 6c, d). Due to the limited IR820 enrichment at the tumor site at a certain time point, the tumor inhibition effect is unsatisfactory in group II. Importantly, during the PTT period, there was no noticeable body weight loss observed in groups I-V (Fig. 6e), affirming the outstanding biocompatibility of GFZI. Furthermore, we conducted histological analysis of excised tumors to assess PTT efficacy. Notable tumor cell necrosis and apoptosis were observed in H&E and TUNEL staining of tumor sections from groups IV and V (Fig. 6f, g), underscoring the suppressive effect of GFZI on tumor growth. H&E staining of main organs and blood index analysis across all groups exhibited no tissue damage and notable differences (Fig. S14). In summary, GFZI achieved highly efficiency FL/PA/ $^{19}\text{F}$  MR trimodal imaging-guided PTT for xenograft A549 lung cancer without obvious toxicity.

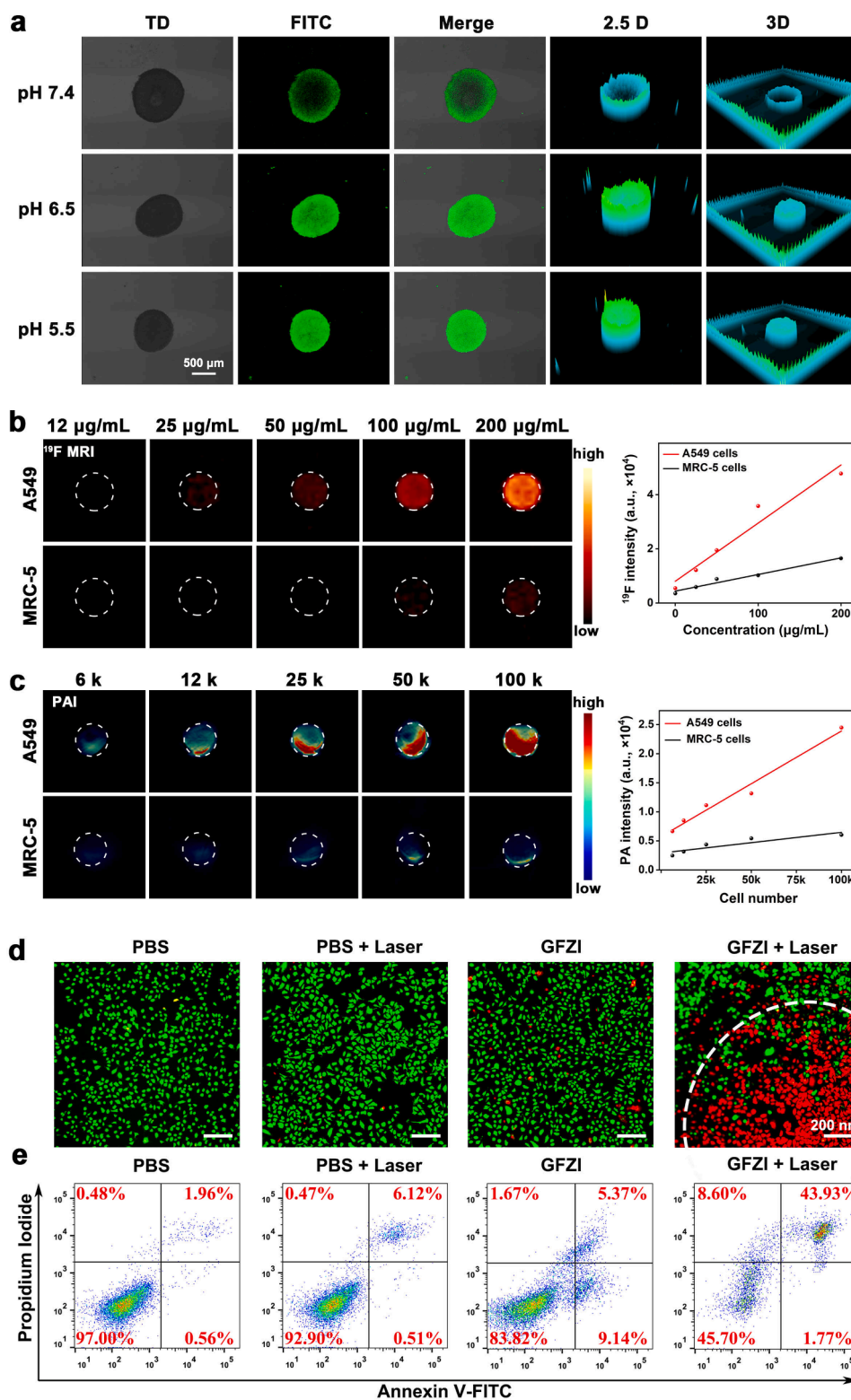


**Fig. 4.** *In vitro* tumor penetration, cellular  $^{19}\text{F}$  MRI/PAI, and the photothermal therapy of GFZI. (a) Tumor penetration images of GFZF in the LLC cell-based multicellular spheroids after respective incubation at pH 7.4, pH 6.5, or pH 5.5 for 2 h. (b)  $^{19}\text{F}$  MRI and the corresponding signal intensity of A549 cells and MRC-5 cells treated with different concentrations of GFZI, respectively. (c) PAI and the corresponding signal intensity of A549 cells and MRC-5 cells treated with GFZI (200  $\mu\text{g/mL}$ ), respectively. (d) CLSM images of calcein-AM/PI labeling of A549 cells incubated with PBS or GFZI (200  $\mu\text{g/mL}$ ) for 6 h, with or without laser irradiation (808 nm, 1.0  $\text{W}/\text{cm}^2$ ). (Scale bar represents 200  $\mu\text{m}$ ). (e) Apoptosis and necrosis analysis of A549 cells incubated with GFZI (200  $\mu\text{g/mL}$ ) under 808 nm laser (1.0  $\text{W}/\text{cm}^2$ ).

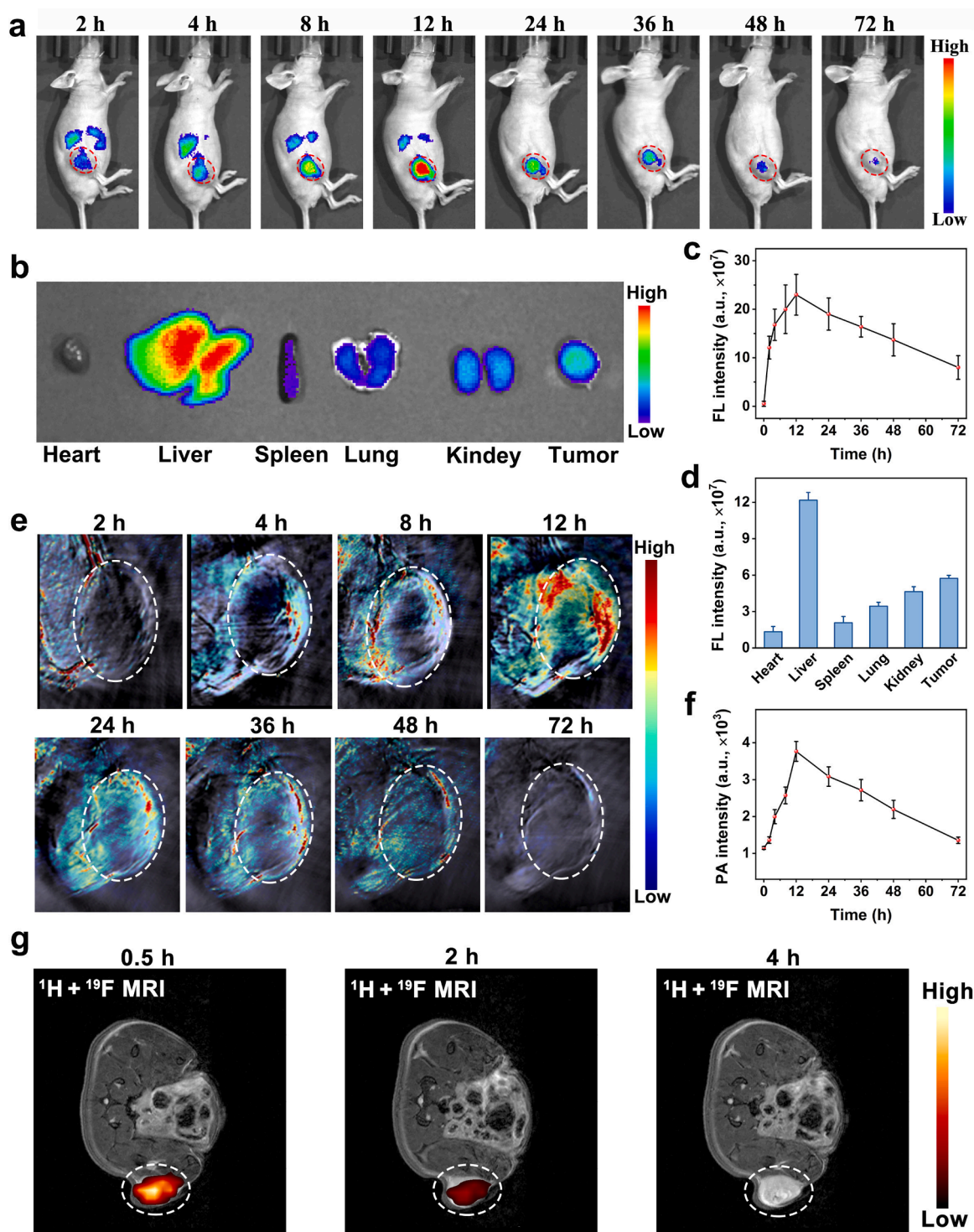


**Fig. 5.** *In vivo* FL/PA/ $^{19}\text{F}$  MR trimodal imaging. (a) Time-based *in vivo* FL images of subcutaneous A549-tumor-bearing mice after *i.v.* injection of GFZI (200  $\mu\text{g}/\text{mL}$ , 100  $\mu\text{L}$ ) and (b) the isolated organs and tumor at 12 h post-injection of GFZI. (c) The corresponding quantification of tumor FL intensity at various times post-injection of the nanoprobe. (d) The corresponding quantification of the isolated organs and tumor FL intensity at 12 h post-injection of GFZI. (e) Time-based *in vivo* PA images of subcutaneous A549-tumor-bearing mice after *i.v.* injection of GFZI (200  $\mu\text{g}/\text{mL}$ , 100  $\mu\text{L}$ ) and (f) the corresponding quantification of tumor PA intensity. (g)  $^{19}\text{F}$  MRI of subcutaneous A549 tumors after intratumoral injection of GFZI (200  $\mu\text{g}/\text{mL}$ , 50  $\mu\text{L}$ ).

#### 4. Conclusion

While nanomaterials offering multimodal-guided cancer therapy have gained traction in biomedicine, the quest for novel nanoplatfroms that respond to the tumor microenvironment to enhance multimodal imaging, thereby improving tumor-to-background ratios, remains a

valuable pursuit. In this endeavor, we have developed a theranostic agent centered around GNRs coated with fluorinated ZIF-8, tailored for FL/PA/MR trimodal imaging-guided PTT in lung cancer. By combining FLI and PAI for high sensitivity, along with  $^{19}\text{F}$  MRI for superior spatial resolution, unlimited penetration depth, and freedom from background interference, we have achieved precise localization of lung cancer. In

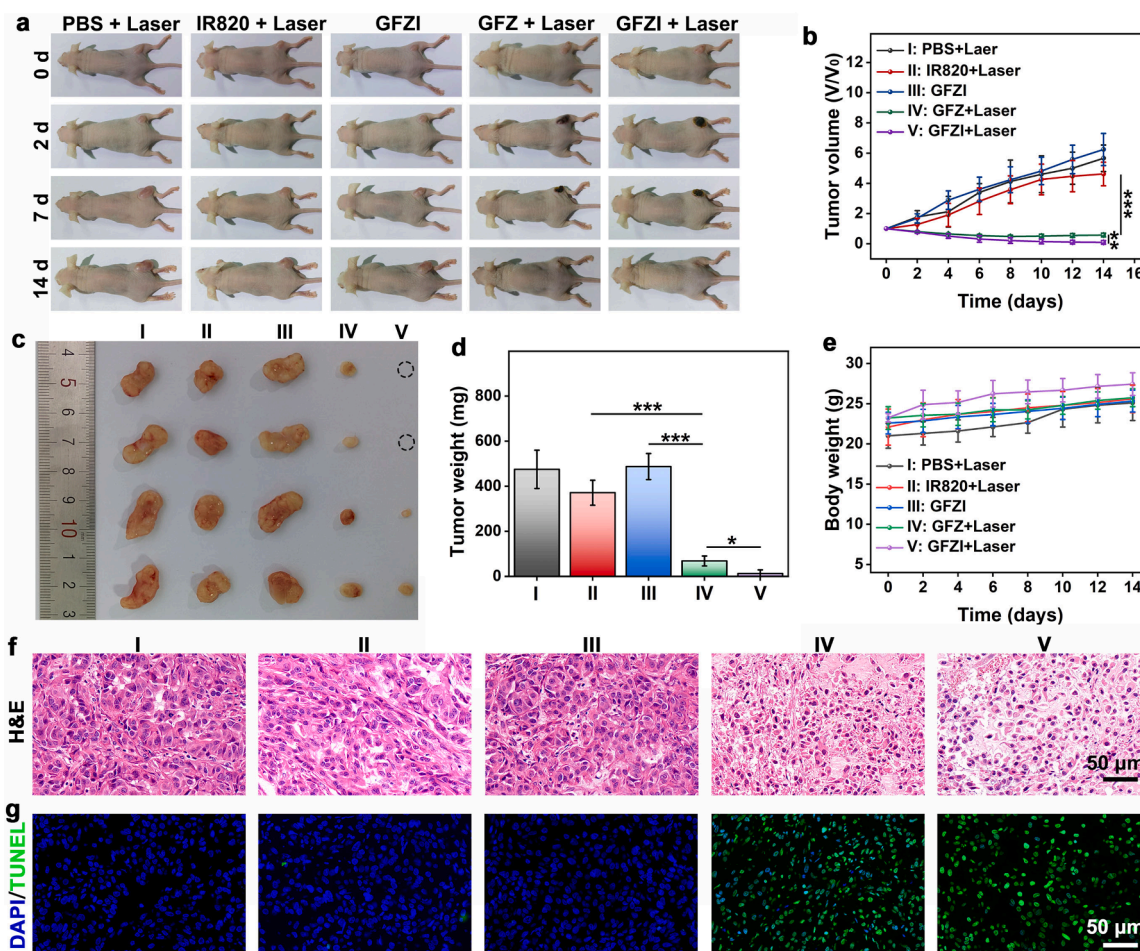


**Fig. 6.** *In vivo* antitumor phototherapy. (a) The representative photographs of A549 tumor-bearing mice in groups I-V on different days. (b) The tumor growth curves, (c) the images of dissected tumors, (d) tumor weight, and (e) body weight curves in the groups I-V. (f) H&E and (g) TUNEL staining of tumor sections (The blue color indicates the cell nucleus and the green color indicates apoptotic cells).

contrast to multimodal probes with "always on" imaging signals, our GFZI nanoplatfrom exhibits acid-activated enhancement in FL/PA/<sup>19</sup>F MR trimodal imaging contrast, a pivotal feature for achieving precision in cancer PTT. Ultimately, we have attained exceptional PTT efficiency in lung cancer, capitalizing on the synergistic photothermal effect of GNRs and IR820. This versatile nanoprobe holds potential for diverse imaging targets, heralding a new and promising era in multimodal molecular imaging.

#### CRediT authorship contribution statement

**Maosong Qiu:** Conceptualization, Validation, Investigation, Methodology, Writing – original draft, Writing – review & editing. **Lei Zhang:** Conceptualization, Writing – review & editing. **Yu Li:** Methodology, Writing – review & editing. **Ruifang Wang:** Investigation, Methodology, Data curation. **Long Xiao:** Methodology. **Shizhen Chen:** Conceptualization, Project administration, Funding acquisition, Writing – review & editing. **Xin Zhou:** Conceptualization, Supervision, Project administration, Funding acquisition, Writing – review & editing.

#### Declaration of competing interest

The authors declare that they have no known competing financial interests or personal relationships that could have appeared to influence the work reported in this paper.

#### Data availability

Data will be made available on request.

#### Acknowledgements

This work was supported by the National Key R&D Program of China (2018YFA0704000), the National Natural Science Foundation of China (U21A20392, 82127802, 21921004, and 81901737), the Hubei Provincial Natural Science Foundation of China (grant no. 05182321). Xin Zhou acknowledges the support from the Tencent Foundation through the XPLOER PRIZE, and Shizhen Chen acknowledges the support from the Young Top-notch Talent Cultivation Program of Hubei Province.

#### Supplementary materials

Supplementary material associated with this article can be found, in the online version, at [doi:10.1016/j.materresbull.2024.112731](https://doi.org/10.1016/j.materresbull.2024.112731).

#### References

- [1] H. Sung, J. Ferlay, R.L. Siegel, M. Laversanne, I. Soerjomataram, A. Jemal, F. Bray, Global cancer statistics 2020: GLOBOCAN estimates of incidence and mortality worldwide for 36 cancers in 185 countries, *CA Cancer J. Clin.* 71 (3) (2021) 209–249.
- [2] J.M. Eberth, One step forward, two steps back: progress and challenges to implementation of lung cancer screening, *Chest* 162 (3) (2022) 505–506.

- [3] M. Oudkerk, S. Liu, M.A. Heuvelmans, J.E. Walter, J.K. Field, Lung cancer LDCT screening and mortality reduction - evidence, pitfalls and future perspectives, *Nat. Rev. Clin. Oncol.* 18 (3) (2021) 135–151.
- [4] D.R. Aberle, A.M. Adams, C.D. Berg, W.C. Black, J.D. Clapp, R.M. Fagerstrom, I. F. Gareen, C. Gatsonis, P.M. Marcus, J.D. Sicks, Reduced lung-cancer mortality with low-dose computed tomographic screening, *N. Engl. J. Med.* 365 (5) (2011) 395–409.
- [5] J. Lin, M. Wang, H. Hu, X. Yang, B. Wen, Z. Wang, O. Jacobson, J. Song, G. Zhang, G. Niu, P. Huang, X. Chen, Multimodal-imaging-guided cancer phototherapy by versatile biomimetic theranostics with UV and  $\gamma$ -irradiation protection, *Adv. Mater.* 28 (17) (2016) 3273–3279.
- [6] L. Liu, J. Zhang, R. An, Q. Xue, X. Cheng, Y. Hu, Z. Huang, L. Wu, W. Zeng, Y. Miao, J. Li, Y. Zhou, H.Y. Chen, H. Liu, D. Ye, Smart nanosensitizers for activatable sonophotodynamic immunotherapy of tumors by redox-controlled disassembly, *Angew. Chem. Int. Ed.* 62 (10) (2023) e202217055.
- [7] B. Li, E. Pang, S. Zhao, G. Deng, S. Wang, B. Wang, J. Wu, G. Niu, X. Song, M. Lan, Aggregation-enhanced photophysical performance of D- $\pi$ -A structured hemicyanine for NIR-II fluorescent and photoacoustic imaging-guided photothermal therapy, *Chem. Biomed. Imaging* 1 (6) (2023) 541–549.
- [8] S. Yang, Y. Wang, Q. Wang, F. Li, D. Ling, DNA-driven dynamic assembly/disassembly of inorganic nanocrystals for biomedical imaging, *Chem. Biomed. Imaging* 1 (4) (2023) 340–355.
- [9] B. Meng, S.L. Grage, O. Babii, M. Takamiya, N. MacKinnon, T. Schober, I. Hutskalov, O. Nassar, S. Afonin, S. Koniev, I.V. Komarov, J.G. Korvink, U. Strähle, A.S. Ulrich, Highly fluorinated peptide probes with enhanced *in vivo* stability for  $^{19}\text{F}$ -MRI, *Small* 18 (41) (2022) e2107308.
- [10] T. Tang, Q. Zhu, S. Liu, H. Dai, Y. Li, C. Tang, K. Chen, M. Jiang, L. Zhu, X. Zhou, S. Chen, Z. Zheng, Z.X. Jiang,  $^{19}\text{F}$  MRI-fluorescence imaging dual-modal cell tracking with partially fluorinated nanoemulsions, *Front. Bioeng. Biotechnol.* 10 (2022) 1049750–1049763.
- [11] L. Zhu, Y. Li, M. Jiang, C. Ke, H. Long, M. Qiu, L. Zhang, C. Ye, X. Zhou, Z.X. Jiang, S. Chen, Self-assembly of precisely fluorinated albumin for dual imaging-guided synergistic chemo-photothermal-photodynamic cancer therapy, *ACS Appl. Mater. Interfaces* 15 (2) (2023) 2665–2678.
- [12] S. Chen, L. Xiao, Y. Li, M. Qiu, Y. Yuan, R. Zhou, C. Li, L. Zhang, Z.X. Jiang, M. Liu, X. Zhou, *In vivo* nitroreductase imaging via fluorescence and chemical shift dependent  $^{19}\text{F}$  NMR, *Angew. Chem. Int. Ed.* 61 (50) (2022) e202213495.
- [13] Y. Zhang, S. Bo, T. Feng, X. Qin, Y. Wan, S. Jiang, C. Li, J. Lin, T. Wang, X. Zhou, Z. X. Jiang, P. Huang, A versatile theranostic nanoemulsion for architecture-dependent multimodal imaging and dually augmented photodynamic therapy, *Adv. Mater.* 31 (21) (2019) e1806444.
- [14] S. Li, W. Jiang, Y. Yuan, M. Sui, Y. Yang, L. Huang, L. Jiang, M. Liu, S. Chen, X. Zhou, Delicately designed cancer cell membrane-camouflaged nanoparticles for targeted  $^{19}\text{F}$  MR/PA/FL imaging-guided photothermal therapy, *ACS Appl. Mater. Interfaces* 12 (51) (2020) 57290–57301.
- [15] E. Swider, K. Daoudi, A.H.J. Staal, O. Koshkina, N.K. van Riessen, E. van Dinther, I. J.M. de Vries, C.L. de Korte, M. Srinivas, Clinically-applicable perfluorocarbon-loaded nanoparticles for *in vivo* photoacoustic,  $^{19}\text{F}$  magnetic resonance and fluorescent imaging, *Nanotheranostics* 2 (3) (2018) 258–268.
- [16] L. Wan, Y. Cao, C. Cheng, R. Tang, N. Wu, Y. Zhou, X. Xiong, H. He, X. Lin, Q. Jiang, X. Wang, X. Guo, D. Wang, H. Ran, J. Ren, Y. Zhou, Z. Hu, P. Li, Biomimetic, pH-responsive nanoplatforms for cancer multimodal imaging and photothermal immunotherapy, *ACS Appl. Mater. Interfaces* 15 (1) (2023) 1784–1797.
- [17] W. Lin, W. Zhang, S. Liu, Z. Li, X. Hu, Z. Xie, C. Duan, G. Han, Engineering pH-responsive BODIPY nanoparticles for tumor selective multimodal imaging and phototherapy, *ACS Appl. Mater. Interfaces* 11 (47) (2019) 43928–43935.
- [18] Z. Dong, L. Feng, Y. Hao, M. Chen, M. Gao, Y. Chao, H. Zhao, W. Zhu, J. Liu, C. Liang, Q. Zhang, Z. Liu, Synthesis of hollow biomineralized  $\text{CaCO}_3$ -polydopamine nanoparticles for multimodal imaging-guided cancer photodynamic therapy with reduced skin photosensitivity, *J. Am. Chem. Soc.* 140 (6) (2018) 2165–2178.
- [19] W. Kang, Y. Tian, Y. Zhao, X. Yin, Z. Teng, Applications of nanocomposites based on zeolitic imidazolate framework-8 in photodynamic and synergistic anti-tumor therapy, *RSC Adv.* 12 (26) (2022) 16927–16941.
- [20] H. Xie, X. Liu, Z. Huang, L. Xu, R. Bai, F. He, M. Wang, L. Han, Z. Bao, Y. Wu, C. Xie, Y. Gong, Nanoscale zeolitic imidazolate framework (ZIF)-8 in cancer theranostics: current challenges and prospects, *Cancers* 14 (16) (2022) 3935–3957.
- [21] Y. Chen, B. Wang, W. Chen, T. Wang, M. Li, Z. Shen, F. Wang, J. Jia, F. Li, X. Huang, J. Zhuang, N. Li, Co-delivery of dihydroartemisinin and indocyanine green by metal-organic framework-based vehicles for combination treatment of hepatic carcinoma, *Pharmaceutics* 14 (10) (2022) 2047–2061.
- [22] M. Liang, W. Zhou, H. Zhang, J. Zheng, J. Lin, L. An, S. Yang, Tumor microenvironment responsive  $\text{T}_1$ - $\text{T}_2$  dual-mode contrast agent  $\text{Fe}_3\text{O}_4$ @ZIF-8-Zn-Mn NPs for *in vivo* magnetic resonance imaging, *J. Mater. Chem. B* 11 (19) (2023) 4203–4210.
- [23] C. Jiang, L. Zhang, X. Xu, M. Qi, J. Zhang, S. He, Q. Tian, S. Song, Engineering a smart agent for enhanced immunotherapy effect by simultaneously blocking PD-L1 and CTLA-4, *Adv. Sci.* 8 (20) (2021) e2102500.
- [24] C. Guo, S. Xu, A. Arshad, L. Wang, A pH-responsive nanoprobe for turn-on  $^{19}\text{F}$ -magnetic resonance imaging, *Chem. Commun.* 54 (70) (2018) 9853–9856.
- [25] T. He, C. Jiang, J. He, Y. Zhang, G. He, J. Wu, J. Lin, X. Zhou, P. Huang, Manganese-dioxide-coating-instructed plasmonic modulation of gold nanorods for activatable duplex-imaging-guided NIR-II photothermal-chemodynamic therapy, *Adv. Mater.* 33 (13) (2021) e2008540.
- [26] Z. Li, R. Bai, J. Yi, H. Zhou, J. Xian, C. Chen, Designing smart iron oxide nanoparticles for MR imaging of tumors, *Chem. Biomed. Imaging* 1 (4) (2023) 315–339.
- [27] C. Li, Y. Zhang, Z. Li, E. Mei, J. Lin, F. Li, C. Chen, X. Qing, L. Hou, L. Xiong, H. Hao, Y. Yang, P. Huang, Light-responsive biodegradable nanorattles for cancer theranostics, *Adv. Mater.* 30 (8) (2018) 1706150.
- [28] L. Chen, Y. Peng, H. Wang, Z. Gu, C. Duan, Synthesis of Au@ZIF-8 single- or multi-core-shell structures for photocatalysis, *Chem. Commun.* 50 (63) (2014) 8651–8654.
- [29] Q. Wang, Y. Yu, Y. Chang, X. Xu, M. Wu, G.R. Ediriweera, H. Peng, X. Zhen, X. Jiang, D.J. Searles, C. Fu, A.K. Whittaker, Fluoropolymer-MOF hybrids with switchable hydrophilicity for  $^{19}\text{F}$  MRI-monitored cancer therapy, *ACS Nano* 17 (9) (2023) 8483–8498.
- [30] Z. Zhang, L. Wang, J. Wang, X. Jiang, X. Li, Z. Hu, Y. Ji, X. Wu, C. Chen, Mesoporous silica-coated gold nanorods as a light-mediated multifunctional theranostic platform for cancer treatment, *Adv. Mater.* 24 (11) (2012) 1418–1423.
- [31] L. Zhao, G. Niu, F. Gao, K. Lu, Z. Sun, H. Li, M. Stenzel, C. Liu, Y. Jiang, Gold nanorods (AuNRs) and zeolitic imidazolate framework-8 (ZIF-8) core-shell nanostructure-based electrochemical sensor for detecting neurotransmitters, *ACS Omega* 6 (48) (2021) 33149–33158.
- [32] S. Chen, M. Qiu, R. Wang, L. Zhang, C. Li, C. Ye, X. Zhou, Photoactivated nanohybrid for dual-nuclei MR/US/PA multimodal-guided photothermal therapy, *Bioconjug. Chem.* 33 (9) (2022) 1729–1740.
- [33] L. Fang, W. Wang, Y. Liu, Z. Xie, L. Chen, Zeolitic imidazole framework coated Au nanorods for enhanced photothermal therapy and stability, *Dalton Trans.* 46 (28) (2017) 8933–8937.